3D experiments on the interaction of a vortex ring with a rising bubble

Cecilia Estepa-Cantero[1,2], Manuel Lorite-Díez[1,2], Javier Ruiz-Rus[2,3], Sébastien Cazin[4], Rocío Bolaños-Jiménez[2,3], Patricia Ern[4] & Carlos Martínez-Bazán[1,2]

1: Dpto. de Mecánica de Estructuras e Ingeniería Hidráulica, Universidad de Granada, Granada, Spain.
2: Instituto interuniversitario de Investigación del Sistema Tierra en Andalucía (IISTA), Universidades de Granada, Jaén and Córdoba, Spain.
3: Dpto. de Ingeniería Mecánica y Minera, Universidad de Jaén, Jaén, Spain.
4: Institut de Mécanique des Fluides de Toulouse (IMFT), CNRS, Toulouse INP and Université de Toulouse, Toulouse, France.
*Corresponding author: mldiez@ugr.es

Keywords: Bubble breakup, Vortex ring, 4D-LPT

ABSTRACT

The interaction between turbulent flows and bubbles is a complex phenomenon ubiquitous in both natural and industrial settings. In this work, we experimentally investigate, from a fundamental perspective, the interaction between a rising bubble and a vortex ring in counterflow. Using time-resolved three-dimensional Lagrangian Particle Tracking (4D-LPT) coupled with tomographic shadowgraphy, we obtain simultaneous measurements of the bubble motion and the surrounding liquid flow. This approach enables detailed observation of the bubble dynamics, deformation, and eventual breakup, as well as the associated fluid motion. We examine several flow configurations by varying the vortex circulation and the Weber number while maintaining a comparable vortex-to-bubble size ratio. Based on these measurements, we classify the interaction events into three categories according to their impact on bubble dynamics and vortex stability over time. Our experiments provide the first investigation of the three-dimensional effects of these interactions, which were overlooked in previous studies. The analysed experiments are divided into three cases: Case I corresponds to a weak interaction in which neither the bubble nor the vortex is significantly affected; Case II describes a regime in which the bubble is captured and advected by the vortex, leading to strong vortex distortion due to the presence of the bubble within its core; and Case III involves a stronger vortex capable of capturing the bubble and breaking it into two fragments without significant loss of energy in the vortex core. The analysis of these results provides insight into the bubble breakup process and the mechanisms responsible for the destabilization of the vortex ring.

1. Introduction

The interaction between bubbles and turbulent vortical structures is fundamental in many engineering and environmental flows, including chemical reactors, ocean mixing, and drag reduction applications (Berkman & Calabrese, 1988; Prince & Blanch, 1990; Melville, 1996). Bubble deformation and breakup strongly affect the transport of mass, momentum, and energy, while turbulence

simultaneously controls bubble dynamics and fragmentation (Balachandar & Eaton, 2010; Spandan et al., 2017).

Bubble breakup in turbulence has traditionally been explained through the Kolmogorov–Hinze framework (Kolmogorov, 1949; Hinze, 1955), which states that breakup occurs when turbulent stresses overcome surface tension forces. This balance is governed by the turbulent Weber number, with the bubbles expected to break primarily through interactions with eddies of comparable size (Chan et al., 2021; Masuk et al., 2021). However, directly investigating this mechanism in turbulent flows remains challenging because of the coexistence of multiple interacting scales.

To simplify the problem, many studies have investigated the interaction between a single bubble and a vortex ring, which serves as an idealized model of a turbulent eddy (Jha & Govardhan, 2015; Martínez-Bazán, 2015). Experimental studies have identified several stages of the interaction, including bubble capture, elongation, breakup, and release (Jha & Govardhan, 2015). These works also demonstrated that deformable bubbles can strongly modify vortex dynamics, reducing both vortex enstrophy and convection speed, particularly at low Weber numbers (Biswas & Govardhan, 2023). Comparisons with rigid particles further highlighted the crucial role of bubble deformability in determining the interaction dynamics (Biswas & Govardhan, 2022).

Numerical simulations have complemented experiments by providing fully three-dimensional information on flow structures and interface evolution (Higuera, 2004; Foronda-Trillo et al., 2021). These simulations revealed mechanisms such as bubble elongation, vortex-core deformation, redistribution of enstrophy among vorticity components, and probabilistic breakup behavior arising from the sensitivity to initial conditions (Foronda-Trillo et al., 2021).

The present work aims to address these unresolved questions through an experimental investigation of bubble–vortex interactions using three-dimensional Lagrangian Particle Tracking (4D-LPT) combined with tomographic reconstruction of the bubble interface. Building upon our recent study of the three-dimensional evolution of vortex-ring structure and bubble deformation during the interaction process (Estepa-Cantero et al., 2026), we examine three representative interaction regimes: weak interaction, capture–transport–release, and bubble breakup (Estepa-Cantero et al., 2026). This approach enables the simultaneous characterization of the three-dimensional flow field and bubble shape, providing detailed insight into the coupling between vortex dynamics and bubble deformation. In the present study, the analysis is further extended through the reconstruction of the instantaneous pressure field from the measured velocity data, yielding direct information on the pressure gradients responsible for bubble deformation and fragmentation. The resulting dataset provides new physical insight into the mechanisms governing bubble–vortex interactions, helps reconcile discrepancies reported in previous studies, and offers valuable benchmark data for the validation of future numerical simulations.

2. Problem description and Experimental details

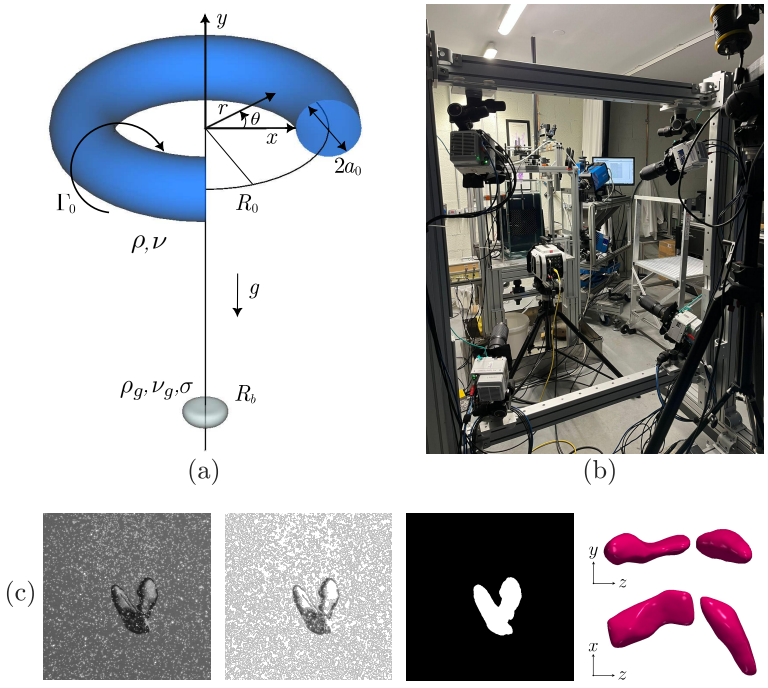


Figure 1. (a) Three-dimensional sketch of the problem, showing the main variables involved and the reference frames. (b) Image of the experimental setup and the distribution of the six cameras used. (c) Bubble detection and reconstruction process.

The study investigates the interaction between a rising bubble and a downward-moving vortex ring in a simplified and controlled configuration (Fig. 1a). The bubble is characterized by its equivalent spherical radius R_b, density ρ_g, viscosity ν_g, and surface tension σ, while the vortex ring is described by its radius $R(t)$, core radius $a(t)$, and circulation $\Gamma(t)$, with initial values R_0, a_0, and Γ_0, respectively. Dimensionless quantities are defined using R_0, R_0^2/Γ_0, and Γ_0/R_0 as characteristic length, time and velocity scales, respectively. Two coordinate systems are employed: a Cartesian system (x, y, z) and a cylindrical system (r, θ, y), allowing an accurate description of the bubble displacement and vortex evolution during interaction.

The dynamics of the problem is governed by four main dimensionless parameters: the Weber number, $We = \rho(\Gamma_0/2\pi R_0)^2/(\sigma/R_b)$, the Reynolds number, $Re = \Gamma_0/\nu$, the vortex-to-bubble size ratio R_0/R_b, and the vortex-core-to-ring radius ratio a_0/R_0. Prior to interaction, the bubble rise regime is determined by the Bond and Galilei numbers, $Bo = \rho g R_b^2/\sigma, Ga = \sqrt{gR_b}\,R_b/\nu$, which define the bubble terminal velocity and associated Reynolds and Weber numbers (Cano-Lozano et al., 2016).

Experiments were conducted at the Institute of Fluid Mechanics of Toulouse (IMFT) using a water tank seeded with fluorescent polyamide particles of 50 μm diameter. The vortex ring was generated through a transient water jet injected from a pressurized reservoir (Gharib et al., 1998). By con-

trolling the injection pressure and valve opening time, the vortex ring characteristics were changed, namely $15 \lesssim R_0 \lesssim 17$ mm, $4 \lesssim a_0 \lesssim 6$ mm, and $94 \lesssim \Gamma_0 \lesssim 146$ cm$^2/s$. In this way, Reynolds number was varied in the range $8 \times 10^3 \lesssim Re \lesssim 15 \times 10^3$, and core-to-ring ratios $a_0/R_0 \approx 0.3$–0.4 were achieved (see Table 1). The bubble was released quasi-statically from the bottom of the tank using a syringe and a conical nozzle, producing bubbles with radius $R_b = 3.65 \pm 0.05$ mm and approximately constant size ratio $R_0/R_b \approx 4.5$. This configuration yielded interaction conditions of $0.4 \lesssim We \lesssim 1$. The measurement volume was positioned at mid-height of the tank to ensure that the vortex ring was fully developed and that the bubble had reached a quasi-terminal rise velocity before interaction. Overall, the experimental setup was specifically designed to simultaneously capture the three-dimensional flow field, vortex evolution, and bubble deformation dynamics during the interaction process.

The interaction was recorded at up to 1496 Hz using six synchronized high-speed cameras arranged to provide multiple viewing angles and optimize tomographic reconstruction (see Fig. 1b). Four frontal cameras and two side cameras were equipped with Scheimpflug mounts and optical filters to minimize distortion and isolate fluorescent particle scattering. Bubble deformation and breakup were simultaneously captured using a tomographic shadowgraphy setup with two LED backlight panels. Flow measurements were obtained using a double-pulsed laser expanded into a volumetric illumination system covering a measurement region of $100 \times 160 \times 80$ mm^3. The liquid velocity field was characterized using 4D Lagrangian Particle Tracking (4D-LPT) based on the Shake-The-Box (STB) (Schanz et al., 2016) algorithm implemented in DaVis 11 from LaVision GmbH software. The flow velocity field was obtained using the four frontal cameras, as the inclusion of two lateral cameras reduced tracking quality due to out-of-focus particles. After accurate camera calibration and particle-based self-calibration (Wieneke, 2018), 80 000–100 000 particle tracks were obtained. Particle velocities were calculated through third-order polynomial fitting over a 15-step window, and the Lagrangian data were interpolated onto an Eulerian grid with a spatial resolution of 0.7–1 mm using binning operation. Instantaneous pressure fields were subsequently reconstructed using the VIC# method (Jeon et al., 2022). This data-assimilation-based flow reconstruction framework enforces the Navier–Stokes equations to obtain physically consistent velocity and pressure fields from the experimental measurements, thereby enabling the analysis of the pressure distribution associated with the interaction process.

To analyse the bubble deformation, the shadow projections of the bubble on each of the 6 cameras were isolated by image segmentation from the greyscale images of the six cameras (see Fig. 1c). The camera arrangement and the calibration were essential for the quality of the tomographic reconstruction. On the one hand, the small angles between each pair of front cameras allowed for an accurate determination of the position of the bubble in a vertical plane. On the other hand, the large angles between the front and lateral cameras provided a variety of points of view, which helps to constrain the reconstruction, avoiding the distortion of the volume due to a lack of depth perception (Tödter et al., 2025). The Multiplicative Line-Of-Sight (MLOS) technique was used for

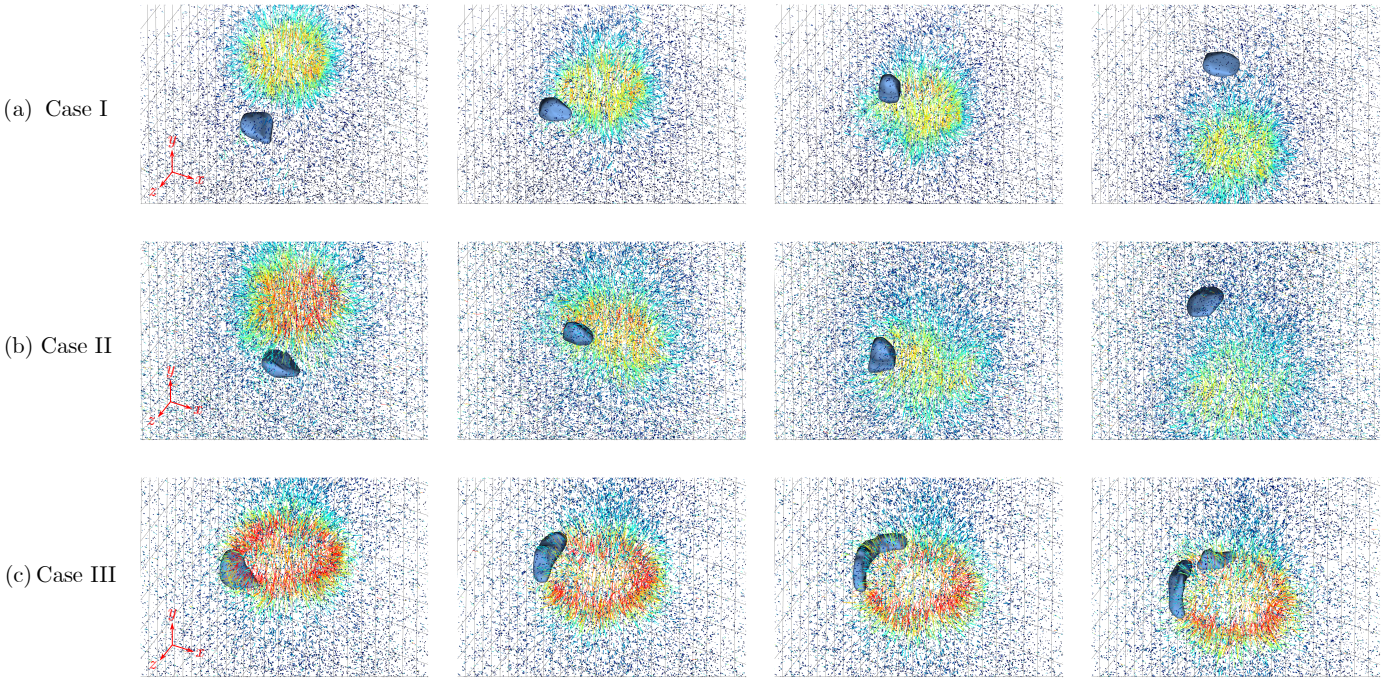


Figure 2. Temporal evolution of the interaction between the bubble and the vortex ring. The pictures show the reconstructed bubble along with the seeding particle trajectories colored by velocity magnitude (black - 0, red - 0.55 m/s). a) Case I, b) Case II and c) Case III.

the reconstruction of the bubble surface. The resulting objects were then corrected by eliminating the potential ghost volumes in the areas covered by the bubble in the lines of sight of the cameras. An additional camera (see Fig. 1b) was used to record the bubble during its formation and detachment process, providing the exact size of the bubbles produced. Excellent agreement was obtained between the reconstructed bubble volume and the axisymmetric volume inferred from the images of that camera, even in the presence of bubble breakup events.

3. Results

The present study focuses on three representative bubble–vortex interaction regimes identified in Jha & Govardhan (2015); Foronda-Trillo et al. (2021); Estepa-Cantero et al. (2026): weak interaction (Case I), capture–transport–release (Case II), and bubble breakup (Case III). Case I corresponds to a low-Weber-number configuration, shown in Fig. 2(a), where the vortex is unable to produce sustained stretching strong enough to significantly deform, trap, or break the bubble. In Case II, illustrated in Fig. 2(b), the Weber number was increased while attempting to keep a_0/R_0 equal to that of Case I, resulting in a stronger interaction in which the coherent vortex ring captures, transports, and deforms the bubble without breakup. The prolonged interaction also leads to substantial vortex-ring attenuation. To investigate the effect of the vortex core ratio, a_0/R_0 was reduced in

Case III while maintaining $We \sim 1$. As shown in Fig. 2(c), the bubble becomes trapped within the vortex core for a relatively long time, where vortex-induced elongation eventually causes breakup into two daughter bubbles. Although the system is deterministic, the dynamics exhibits stochastic behaviour. Together with the lower value of a_0/R_0 in Case III, this may explain why breakup occurs in Case III despite its Weber number being slightly smaller than that of Case II (see Table 1).

Table 1. Dimensionless parameters describing the different types of interactions studied.

Case	Description	R_0/R_b	a_0/R_0	We	Bo	Ga
I	Weak interaction	4.3	0.37	0.41	1.57	618.5
II	Capture, drag and release	4.5	0.38	1.00	1.81	690.5
III	Bubble breakup	4.2	0.28	0.77	1.75	671.5

3.1. Bubble deformation

Figure 3 shows the temporal evolution of the bubble surface normalized with its initial value, S/S_b, during its interaction with the vortex ring, together with different views of the reconstructed bubble shape at three selected instants. We define the beginning of the interaction, $t = 0$, as the moment when the bubble deviates from its rising path due to the presence of the vortex ring, and its end, t_f, as the moment when the bubble resumes its stationary rise and leaves the ring's influence. The interaction time is therefore $t = t_f$ (marked in grey in Fig. 3). The first selected instant (red) corresponds to the initial stage of the bubble rise, before any influence from the counter-flowing vortex ring. The second instant (blue) is chosen during the interaction, and the last one is taken after the interaction (Cases I and II) or after breakup (Case III). In Case I, the bubble undergoes only moderate, reversible deformation and passes relatively quickly through the ring (see Fig. 3a). In contrast, the stronger vortex in Case II (higher We) traps the bubble for a longer time, promoting sustained interface stretching and deformation. Nevertheless, vortex-induced stresses remain insufficient to trigger the extreme elongation and interfacial thinning processes required for breakup. As a result, the bubble preserves its integrity and eventually relaxes towards a less deformed configuration, ultimately escaping from the weakened vortex ring. This behavior highlights the strongly coupled nature of the interaction, in which the vortex ring deforms and transports the bubble, while the bubble simultaneously alters and progressively weakens the vortical structure (Estepa-Cantero et al., 2026). Finally, in Case III the bubble experiences intense deformation, leading to substantial interface stretching and eventual breakup. In fact, before fragmentation occurs, the bubble surface exceeds twice its initial value, indicating the strong elongation and interfacial thinning generated by the vortex-ring-induced stresses. The bubble then splits into two daughter bubbles of different sizes, which remain trapped inside the vortex core throughout the recorded experiment (see Figs. 2, 3).

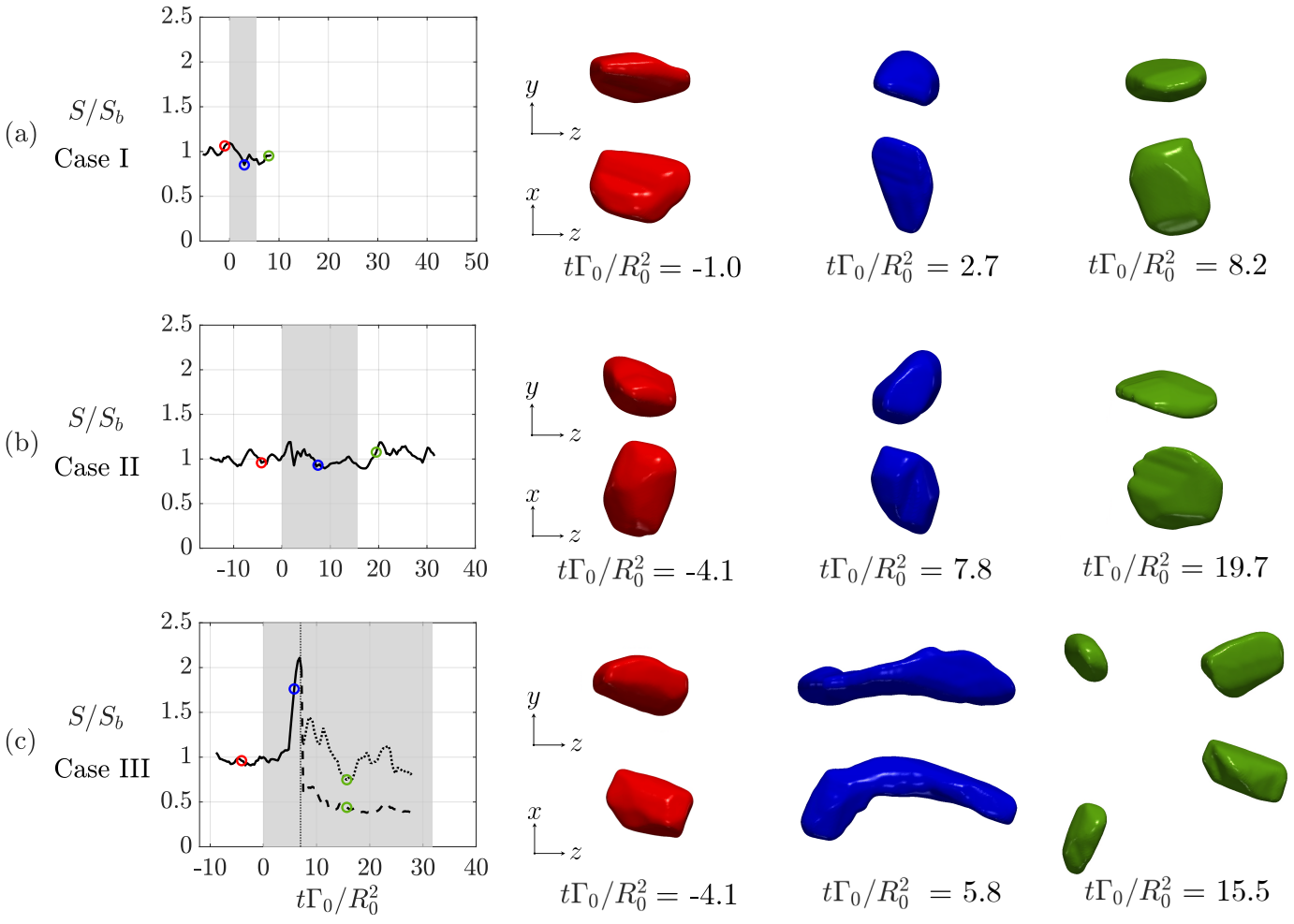


Figure 3. Temporal evolution of the bubble surface ratio, S/S_b, for the cases regarding (a) weak interaction, (b) capture, drag and release, and (c) bubble breakup, respectively. Dotted and dashed lines in (c) show daughter bubbles' velocities and surfaces, respectively. The interaction time is highlighted in grey. The reconstructed bubble at two perpendicular views is also depicted for the selected instants highlighted with red, blue and green circles.

3.2. Flow effects

The canonical flow associated with the initial vortex ring is disrupted to different extents, depending on the case, during the interaction with the rising bubble. To highlight the effects of the bubble on the vortex ring and the surrounding fluid, Fig. 4 presents the normalized probability density functions (PDFs) of the cylindrical liquid velocity components over the entire measurement volume for the three cases and the three selected instants highlighted in Fig. 3. All PDFs exhibit a narrow central peak around zero velocity, corresponding to quiescent seeding particles located far from the bubble–vortex interaction region; this sharp peak arises because the vortex ring occupies only a small fraction of the measurement volume, while most of the domain contains nearly stagnant fluid. The PDFs at the first instant (red) exhibit similar shapes for all cases, since they correspond to stages where the bubble has not yet significantly altered the vortex-ring dynamics,

and thus they represent velocity distributions unaffected by the interaction. The main differences arise from the different circulation and core sizes of the vortex rings in each case. Regarding the interaction regimes, Case I shows nearly identical PDF shapes at the three selected instants, reflecting the weak interaction between the bubble and the vortex ring. In Case II, the stronger vortex captures and retains the bubble for a longer time, leading to a significant weakening of the vortex after the interaction. This effect is reflected in the PDFs, whose velocity distributions become narrower at $t\Gamma_0/R_0^2 \simeq 20$ (green). These PDFs also display a larger proportion of small velocities after the interaction, which may indicate the breakdown of strong coherent vortices, such as the vortex ring and the bubble wake, into smaller vortical structures. The broad tails observed in the axial velocity before interaction are associated with the strong velocity gradients generated by the coherent vortex ring. As the bubble remains trapped inside the vortex core, momentum is progressively transferred from the ring to the surrounding fluid, leading to a reduction of the extreme velocity events and therefore to narrower velocity distributions. However, despite the occurrence of bubble breakup, the velocity PDFs in Case III exhibit smaller changes between the initial and final stages than those observed in Case II. This behaviour suggests that the vortex ring retains a substantial fraction of its initial momentum after the interaction. Numerical simulations by Foronda-Trillo et al. (2021) also showed that bubble breakup does not necessarily lead to vortex ring weakening. In fact, the vortices capable of producing bubble breakup in Foronda-Trillo et al. (2021) remained almost unaffected after the interaction. Notice that, interestingly, the azimuthal velocity PDFs remain comparatively unchanged during and after the interaction, particularly in Case III. This observation suggests that bubble breakup does not significantly alter the rotational motion within the vortex core, in agreement with the numerical findings of Foronda-Trillo et al. (2021).

3.3. Pressure evolution during the interaction process

The interaction between the bubble and the vortex ring is governed by the parameters listed in Table 1. Since the size ratio remains approximately constant across all cases, the problem is mainly controlled by We and a_0/R_0. The Weber number compares inertial effects, based on the radial pressure gradient induced by the vortex, with the bubble surface tension. However, the interaction outcome cannot be fully described by the Weber number alone, as it is also influenced by the spatial distribution of the vortex-induced stresses within the vortex core. Recent three-dimensional measurements have shown that thinner vortex cores can promote more localized interface stretching and deformation, thereby increasing the likelihood of breakup even for comparable Weber numbers (Estepa-Cantero et al., 2026). In this regard, the reconstruction of the instantaneous pressure field provides information not only on the stresses acting on the bubble interface, but also on the evolution of the vortex-ring dynamics during the interaction. In particular, pressure gradients govern the deformation, trapping and eventual breakup of the bubble, while the progressive

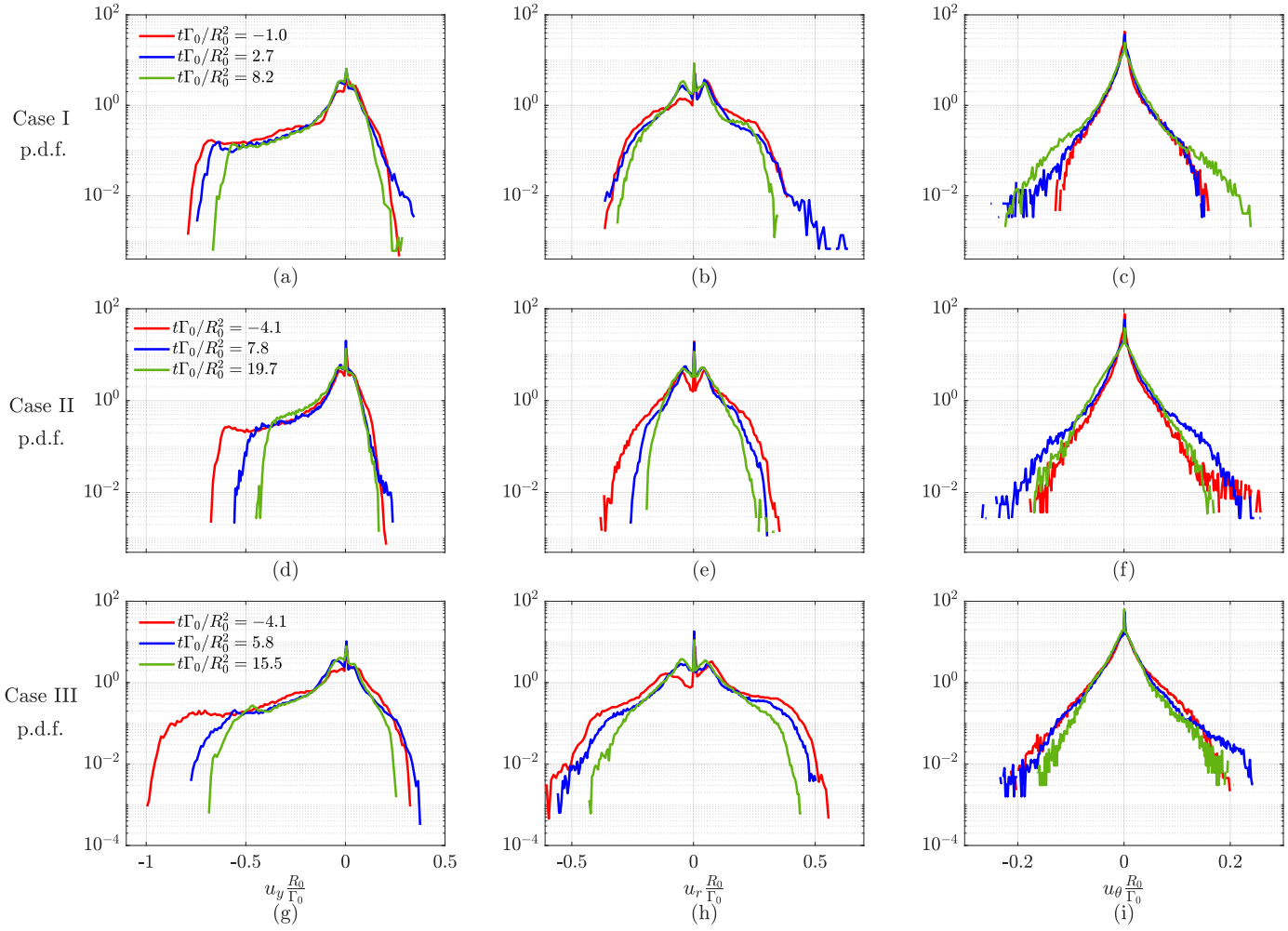


Figure 4. Normalized PDFs for the three velocity components at three selected instants. First row: Case I, second row: Case II and third row: Case III.

attenuation of the low-pressure core reflects the weakening of the vortex ring as momentum and kinetic energy are redistributed throughout the flow. To the best of our knowledge, this is the first time that the pressure field has been experimentally obtained for this three-dimensional problem. Figure 5 analyzes the interaction through the pressure distribution inside the vortex. The bubble is attracted toward the vortex core due to the negative pressure within it. In Case I, the pressure gradient is not strong enough to produce an intense or sustained interaction, and the bubble quickly escapes after interacting with the vortex. In Case II, due to an initial lower pressure in the vortex core, the bubble remains inside the vortex core for a longer time but does not undergo strong deformation. Instead, it reduces the vortex ring inertia and weakens the pressure gradient (see Fig. 5). Finally, in Case III, the vortex strongly elongates the bubble in the azimuthal direction, ultimately leading to the bubble breakup. This elongation results from the azimuthal pressure distribution inside the vortex. As shown in Fig. 5, the bubble remains in regions of relatively higher pressure and progressively migrates toward the minimum pressure zone. Notice that the maximum pressure

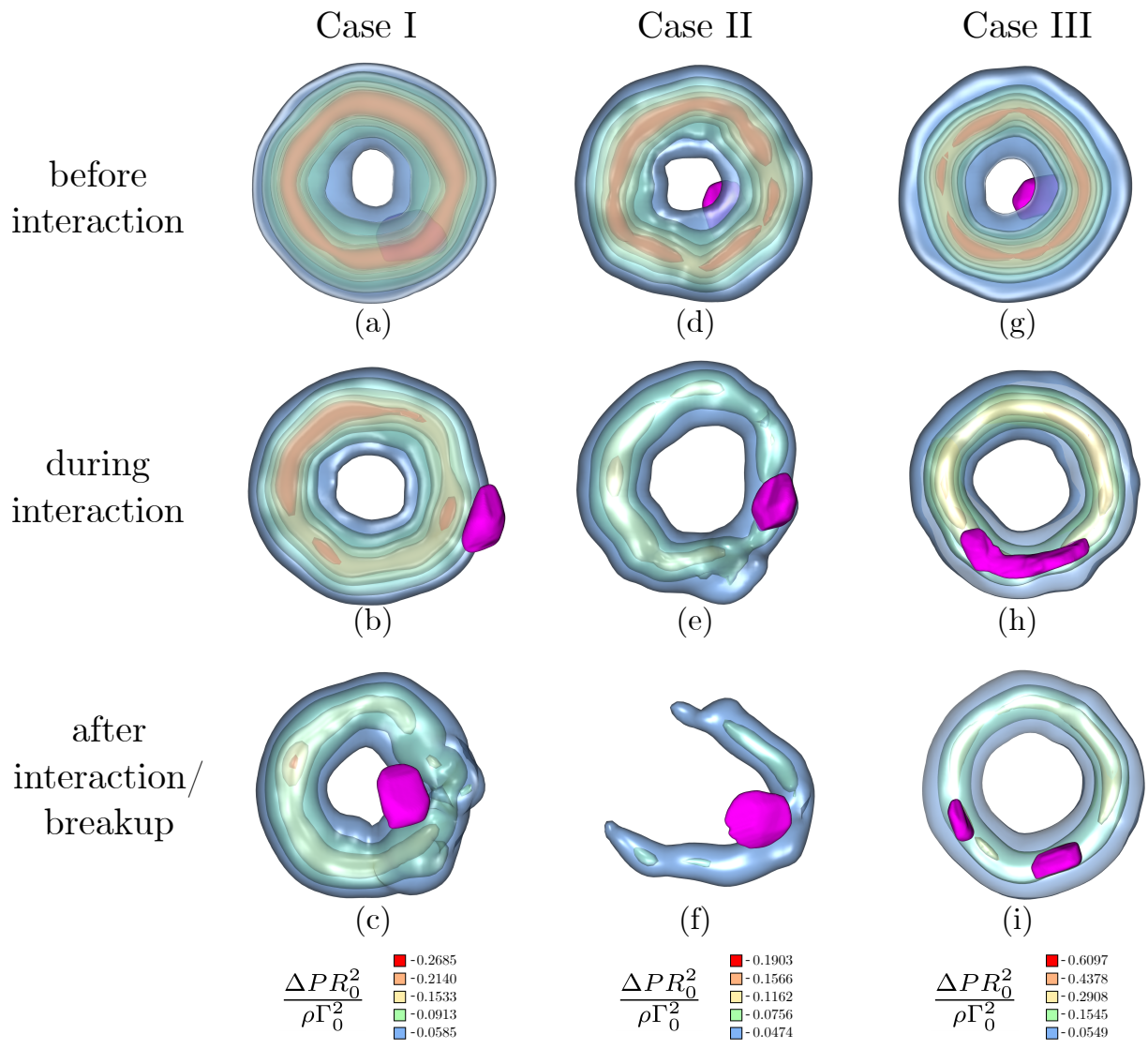


Figure 5. Isocontours of pressure distribution and bubble position at three selected instants (top view). First column: Case I, second column: Case II, and third column: Case III. Bubble surface is highlighted in magenta.

difference in Case III is approximately twice that observed in Case I. Finally, it can be observed that the pressure distribution reveals a clear correlation between vortex-induced pressure gradients and the bubble surface evolution shown in Fig.3. Cases I and II exhibit moderate pressure differences leading to reversible deformations, whereas the larger pressure gradients measured in Case III are associated with the strong interface stretching that leads to the bubble breakup.

4. Conclusions

The interaction between a counter-flowing rising bubble and a transitional vortex ring has been experimentally investigated using a time-resolved tomographic approach. Based on 4D-LPT mea-

surements of the flow field (velocity distribution and pressure levels) and volumetric reconstruction of the bubble surface (deformation and breakup analysis), three representative interaction regimes have been analyzed: weak interaction (Case I), capture, drag, and release (Case II), and bubble breakup (Case III).

The main features of the interaction between the vortex structure and bubble deformation reveal that, in Case I, the bubble only slows down during the interaction, leaving the vortex structure almost unaltered. In Case II, bubble dragging does not produce significant bubble deformation, but weakens the vortex ring, modifying the three-dimensional velocity distribution, and substantially reducing the radial pressure gradient. Finally, in Case III, the vortex induces a strong nonlinear deformation of the bubble, eventually leading to breakup. However, this process does not significantly alter the vortex velocity and pressure.

Acknowledgements

The authors acknowledge the CNRS Research Federation FERMaT (FR3089) for giving access to the 4D-LPT system at IMFT and thank H. Ayroles, C. Perez and L. Mouneix for the technical support provided for the experimental setup at IMFT. This work was partly supported by projects PID2023-151343NB-C32 and PID2022-140433NA-I00, financed by MCIN/AEI/10.13039/50110001-1033/ FEDER, UE. J.R.R. acknowledges the financial support provided by the European Union through the NextGenerationEU Fellowship UJAR06MS. R.B.J would like to acknowledge the project R1C_2025_011 funded by the Research and Knowledge Transfer Internal Plan of the University of Jaén. C.E.C. would like to thank the Spanish Ministry of Universities for the financial support provided by the Fellowship FPU20/02197. M.L.D. also acknowledges the grant RYC2023-044496-I financed by MICIU/AEI /10.13039/501100011033 and FSE+. P.E. and S.C. acknowledge financial support from Toulouse INP, international program ETI.

References

Balachandar, S., & Eaton, J. K. (2010). Turbulent dispersed multiphase flow. *Annu. Rev. Fluid Mech.*, *42*, 111–133.

Berkman, P. D., & Calabrese, R. V. (1988). Dispersion of viscous liquids by turbulent flow in a static mixer. *AIChE J.*, *34*(4), 602–609.

Biswas, S., & Govardhan, R. N. (2022). Interaction of a rigid buoyant sphere and a deforming bubble with a vortex ring: The role of deformability. *Phys. Rev. Fluids*, *7*(9), 094302.

Biswas, S., & Govardhan, R. N. (2023). Vortex ring and bubble interaction: Effects of bubble size on vorticity dynamics and bubble dynamics. *Phys. Fluids*, *35*(8).

Cano-Lozano, J. C., Martínez-Bazán, C., Magnaudet, J., & Tchoufag, J. (2016). Paths and wakes of deformable nearly spheroidal rising bubbles close to the transition to path instability. *Phys. Rev. Fluids*, *1*(5), 053604.

Chan, W. H. R., Johnson, P. L., & Moin, P. (2021). The turbulent bubble break-up cascade. Part 1. Theoretical developments. *J. Fluid Mech.*, *912*, A42.

Estepa-Cantero, C., Lorite-Díez, M., Ruiz-Rus, J., Cazin, S., Bolaños Jiménez, R., Ern, P., & Martínez-Bazán, C. (2026). Three-dimensional experimental investigation of the interaction between a rising bubble and a vortex ring. *Zenodo*. (Preprint, under review at Journal of Fluid Mechanics) doi: 10.5281/zenodo.19001573

Foronda-Trillo, F. J., Rodríguez-Rodríguez, J., Gutiérrez-Montes, C., & Martínez-Bazán, C. (2021). Deformation and breakup of bubbles interacting with single vortex rings. *Int. J. Multiphase Flow*, *142*, 103734.

Gharib, M., Rambod, E., & Shariff, K. (1998). A universal time scale for vortex ring formation. *J. Fluid Mech.*, *360*, 121–140.

Higuera, F. J. (2004). Axisymmetric inviscid interaction of a bubble and a vortex ring. *Phys. Fluids*, *16*(4), 1156–1159.

Hinze, J. O. (1955). Fundamentals of the hydrodynamic mechanism of splitting in dispersion processes. *AIChE J.*, *1*(3), 289–295.

Jeon, Y. J., Müller, M., & Michaelis, D. (2022). Fine scale reconstruction (vic#) by implementing additional constraints and coarse-grid approximation into vic+. *Experiments in Fluids*, *63*(4), 70.

Jha, N. K., & Govardhan, R. N. (2015). Interaction of a vortex ring with a single bubble: bubble and vorticity dynamics. *J. Fluid Mech.*, *773*, 460–497.

Kolmogorov, A. (1949). On the breakage of drops in a turbulent flow. In *Dokl. akad. navk. sssr* (Vol. 66, pp. 825–828).

Martínez-Bazán, C. (2015). About bubbles and vortex rings. *J. Fluid Mech.*, *780*, 1–4.

Masuk, A. U. M., Salibindla, A. K. R., & Ni, R. (2021). Simultaneous measurements of deforming hinze-scale bubbles with surrounding turbulence. *J. Fluid Mech.*, *910*, A21.

Melville, W. K. (1996). The role of surface-wave breaking in air-sea interaction. *Annu. Rev. Fluid Mech.*, *18*, 279–321.

Prince, M. J., & Blanch, H. W. (1990). Bubble coalescence and break-up in air-sparged bubble columns. *AIChE J.*, *36*, 1485–1499.

Schanz, D., Gesemann, S., & Schröder, A. (2016). Shake-The-Box: Lagrangian particle tracking at high particle image densities. *Exp. Fluids*, *57*(5), 70.

Spandan, V., Verzicco, R., & Lohse, D. (2017). Deformable ellipsoidal bubbles in Taylor-Couette flow with enhanced Euler-Lagrangian tracking. *Phys. Rev. Fluids*, *2*, 104304.

Tödter, S., Sagar, H., Thome, M., Michaelis, D., Mannel, K., Neugebauer, J., … Schellin, T. E. (2025). Application of tomographic reconstruction techniques to quantify multiphase flows during sloshing model tests. *Ocean Eng.*, *317*, 120034.

Wieneke, B. (2018). Improvements for volume self-calibration. *Meas. Sci. Technol.*, *29*(8), 084002.